https://doi.org/10.48048/tis.2025.9002

Preparation and Characterization of CuO/ZnO Nanostructures Thin Films using Thermal Evaporation for Advanced Gas Sensing Applications

Ahmed A. Jabber* and Ali R. Abdulridha

Department of Physics, College of Education for Pure Sciences, University of Babylon, Hilla 51002, Iraq

(*Corresponding author's e-mail: ahd090000@gmail.com)

Received: 14 September 2024, Revised: 14 October 2024, Accepted: 16 November 2024, Published: 10 January 2025

Abstract

In the current study, thin films of copper oxide (CuO-based) and zinc oxide (ZnO-doped) were fabricated using the thermal evaporation technique. The evaporation process occurs at 1×10^{-7} bar pressure and 0.5 nm s^{-1}deposition rate. At room temperature (RT), the film thickness is (50 ± 0.2) nm and is deposited on glass substrates. After deposition, films are annealed at 573 K for 2 h. XRD analysis proved that CuO is monoclinic wurtzite-type with the presence of ZnO in the prepared films. This process yielded films with a homogeneous surface, as confirmed by AFM. As ZnO doping increased, roughness increased by 25 %, the root mean square value increased by 23.55 %, and the average grain diameter increased by 65.94 %. The FE-SEM analysis showed equally scattered (CuO/ZnO) nanoparticles (NPs). The optical characteristics of (CuO/ZnO) show that the absorbance and absorption coefficient increase with ZnO content. Transmittance and energy band gaps reduced from 0.889 to 0.742 at λ = 360 nm and 3.608 to 3.504 eV, respectively, as ZnO concentrations increased. The greatest reported sensitivity to NO_2 at a concentration of 0.20 wt.% was 47.06 % at operating temperature of 100 °C. This sensitivity was achieved within a reaction time of 36 s and a recovery time of 19.8 s. The sensitivity of the sample (0.20 wt.%) normally decreases with increasing temperature. This suggests that the gas sensor can interact with NO_2 gas without needing any activation energy and that the interaction is based on physical adsorption and polarity. Nevertheless, the sensitivity of the (Pure, 0.08, and 0.14) wt.% samples exhibited a positive correlation with temperature within a specific range. The findings regarding the structural and conductive properties of (CuO/ZnO) thin films have potential applications in diverse optoelectronics devices and gas sensors.

Keywords: Nanocomposites, Thin films, Thermal evaporation, XRD, FESEM, Gas sensor

Introduction

Nanotechnology is an important part of modern research, especially, when it comes to both making nanoparticles with different shapes, sizes, and chemical makeups and finding ways to use them to help people. The technology can be used in many different areas, especially in the medical, chemical, and physical industries. The catalytic activity and other properties of the nanocomposites, such as their ability to kill bacteria, are related to the nanocomposites. Nanocomposites are interesting because of their unique magnetic, electrical, optical, catalytic, and antimicrobial properties, as well as the way they are made and used [1]. A nanomaterial is a substance that falls within the size range of 1 to 100 nanometers. Nanoparticles possess diminutive particle dimensions, a limited range of pore sizes, minimal aggregation, and exceptional dispersion [2]. Nanomaterials have a wide range of applications, including gas sensing, beauty product formulation, medication development, display technology, battery production, paint manufacture, catalysis, food engineering (including processing, safety, and packaging), farming practices, energy storage and conversion, and building [3].

In the last century, the field of nanotechnology has experienced significant growth. Currently, numerous types of study are interconnected with nanotechnology to varying degrees. Nanotechnology involves the manipulation and utilization of materials and devices at the nanoscale, which involves altering their dimensions and form. The prefix "nano" is

employed at the onset of every stream utilized, including in commercial promotions, as a keyword [4]. The applications of nanotechnology are extensively employed across various scientific and technological domains [5]. Nanoscience studies atom organization and fundamental qualities at the nanoscale, unlike nanotechnology. Nanotechnology manipulates matter at the atomic level to generate new nanomaterials with unique features [6]. Nanomaterials are substances that have a size of less than 100 nm in at least 1 dimension. In other words, this implies that they possess a substantial amount of a considerably smaller micro size. Nanomaterials have dimensions that are one billionth of a meter, often measuring around 10^{-9} m. The physicochemical properties of nanoparticles are inherently connected to the size and shape of the bulk material.

Nanocomposites can be made in many ways, including chemical, physical, biological, etc. Nanomaterials' unique and customizable features have fascinated researchers throughout the globe, and their potential is being studied in disciplines such as medical treatments and diagnostics, drug transport, antibacterial nanomedicine, photocatalysis, catalysis, and energy generation [7,8]. At the nanoscale, the morphology and dimensions of nanomaterials give rise to unique properties and enhanced functionalities [9]. Metal oxides are highly significant in numerous applications because of their propensity to absorb light [10]. Thus, adding metal oxide nanoparticles to glass substrates. Metal and metal oxide nanoparticles are used in catalysis, molecular sensing, and environmental remediation [11]. Various applications of metal oxides have been explored [12,13]. The early transition metal oxides showed catalytic, electro-optic, electromechanical, Ferroelectricity, and wave density charging features [14]. These features allow selective oxidation and dehydration. These metal oxide materials can be employed. Their unique physicochemical properties have also garnered biomedical research attention [15].

The scientific community has become more interested in recent efforts to produce semiconductor oxide materials. Due to its electrical and optical properties, CuO is a commonly utilized semiconductor. This oxide is a p-type semiconductor with a band gap of 3 to 3.62 eV [16-18]. CuO has been recognized as a technologically significant material due to its various uses in advanced science and technology, such as gas sensors [19], sun photovoltaics, heterogeneous catalysis, lithium-ion electrodes, high-temperature superconductors, field emission emitters [20] and so forth. The authors assert that the catalytic properties of CuO thin films have not been thoroughly investigated previously. The material's nontoxicity, chemical stability, high specific surface area, and ease of production rendered it the preferred choice. Multiple recognized methods exist for the fabrication of CuO thin films, such as chemical bath deposition [21], derived from a singular source precursor [22]. Chemical vapor deposition, sputtering, spray pyrolysis, spin coating, electrochemical deposition, for instance. Moreover, it is appealing as a selective solar absorber due to its high solar absorbance and moderate thermal emittance. CuO films exhibit inherent p-type conductivity attributed to copper vacancies within the structure [23,24]. A significant benefit of utilizing CuO in device applications is its non-toxicity and the abundant availability of its elements [25].

ZnO is produced annually at around 1.5 million tons and has been utilized throughout history [26]. ZnO is stable, piezoelectric, and optically excellent. These technologies include photovoltaic cells, gas sensors, transparent conductive materials, surface acoustic wave devices, and piezoelectric transducers. Recent electronic innovations feature a few applications that show their promise [27]. Thin ZnO sensors, made from oxide semiconductors with a high band gap, can be utilized to detect certain lights and gasses. Regarding complex applications such as window layers, ZnO is widely utilized as a transparent conducting oxide in heterojunction solar cells, as well as in heat mirrors and piezoelectric devices. ZnO has a high direct optical energy gap of 3.3 eV, which allows solar radiation to pass through it mostly. In addition, the plentiful presence of ZnO in nature, which reduces its expense, and its strong ability to block UV radiation allows for its utilization in a wide variety of products and procedures [28]. There are a lot of researches in recent years that explore the using of CuO and ZnO nanoparticles for gas sensor applications [29-32].

This research explores several doping techniques to enhance the sensing capabilities of ZnO-based materials. A summary of the recent advancements is

provided, along with the most recent discoveries are evaluated. Emphasis is specifically put on Unraveling the fundamental mechanism behind the sensing behavior. Our projections for the future of sensing materials based on ZnO and related technologies are built upon the latest advancements Discoveries in the domain.

Materials and methods

Specific experimental approaches are used to produce and analyze CuO thin films made of CuO and improved with various ZnO concentrations (0.08, 0.14, 0.20 wt.%). Thermal evaporation on glass substrates produced these films. The Edward C 306 thermal evaporator model is to be used. The pressure during evaporation was approximated to 10^{-7} mbar. The distance between the source and the substrate was kept at 15 cm. The samples are annealed at 573 K then morphology and structure will be examined using X-ray diffraction (XRD), Scanning Electron Microscope (FESEM), and Atomic Force Microscope (AFM). Optical. Thin film optical measurements include absorbance (A), transmittance (T), coefficient of sorption (α), optical energy gap (E_g), refractive index (n), and optical conductivity (σ_{op}) A Shimadzu UV-1800 A° spectrophotometer with a dual-beam laser measured 200 - 1100 nm. The equation for absorbance is the ratio of light intensity absorbed by a material (I_A) to light intensity incident on it (I_0) [33]:

$$A = I_A/I_0 \quad (1)$$

The transmittance (T) is calculated by dividing the transmitted light intensity by the incident ray intensity on a surface. Use the formula to calculate the ratio [33]:

$$T = exp[-2.303\,A] \quad (2)$$

The absorption coefficient refers to the decrease in the energy flow of an incoming ray as a percentage of a unit distance, depending on the direction of wave diffusion. The absorption coefficient (α) is influenced by photon energy, material properties, and the nature of electronic transitions. This equation demonstrates the influence of these parameters on the absorption coefficient (α) [34]:

$$E = h\upsilon \quad (3)$$

The equation below represents transmittance. In cases where incident photon energy is below the forbidden threshold:

$$T = (1-R)^2.e^{-\alpha t} \quad (4)$$

The severity of the occurrence. The intensity of the transmitted ray (I) can be determined using Lamber's law when a ray (I_o) strikes the film material with a thickness (t) [34]:

$$I = I_o \exp(-\alpha t) \quad (5)$$

The absorption coefficient is quantified in units of cm^{-1}.

$$\alpha t = 2.303\, log\, {}^{I}/_{I_o} \quad (6)$$

The logarithm of the ratio of the intensity of transmitted light (I) to the initial intensity of incident light (I_o) is denoted as the absorbance (A).

The absorption coefficient can be determined by applying the following equation [35]:

$$\alpha = 2.303\,(\frac{A}{t}) \quad (7)$$

This study shows direct information transfer between conduction routes. Band (C.B) perfectly extends over valence. band It can be calculated using the equation [36]:

$$\alpha h\upsilon = B(h\upsilon - E_{g\,opt})^r \quad (8)$$

The constant B is constant regardless of material occurrence. Photon frequency is determined by the exponential constant, r, which varies by transition type. An allowed direct transition has r = 1/2, while a forbidden direct transfer has r = 3/2.

$$n = c/\mathrm{v} \quad (9)$$

The coefficient of refraction is (n), while the vacuum speed of light is (c). In a material medium, (v)

denotes light velocity. Equation for refractive index [37]:

$$n = \frac{1+\sqrt{R}}{1-\sqrt{R}} \quad (10)$$

Calculating optical conductivity (σ_{op}) involves the following equation [38]:

$$\sigma_{op} = \alpha nc/4\pi \quad (11)$$

where c is the velocity of light and α is the absorption coefficient.

The sensor response (S) is the ratio of the change in resistance (R_g – R_a) when subjected to target analytics to the sensor's air resistance (Ra) [39].

$$S\ (\%) = \left|\frac{R_a - R_g}{R_g}\right| \times 100\ \% \quad (12)$$

where R_g and R_a represent the resistances of the sensor while exposed to analyte gas and when exposed to air, respectively.

The response time and recovery time curves are determined by calculating the time it takes for the system to respond and recover at severe operating temperatures ranging from RT °C to 200 °C, using specific equations [40,41]:

$$Response\ time = \left|t_{\text{gas (on)}} - t_{\text{gas (off)}}\right| \times 0.9 \quad (13)$$

$$Recover\ time = \left|t_{\text{gas (off)}} - t_{\text{gas (recover)}}\right| \times 0.9 \quad (14)$$

Sensor resistance changes owing to adsorbed gas are used to detect semiconducting metal oxide sensors. Eq. (12) calculates the temperature-specific sensitivity factor (S%). Surface roughness, porosity, wide surface area, and high oxidation rate improve sensing film sensitivity [39].

Results and discussion

XRD Diffraction

The X-ray diffraction (XRD) analysis of ZnO and CuO nanopowders are shown in **Figures 1** and **2**, respectively. **Figure 3** illustrates XRD patterns of both pure CuO and ZnO-doped CuO thin films annealing at 573 K. The spectrum exhibits one peak at 35.55 ° (⁻111) corresponding to CuO (as per JCPDS card No. 96-901-5925), indicating that the crystal structure of CuO is monoclinic wurtzite-type, with the crystals aligned along the c-axis [42]. For, CuO with different ratios of ZnO showed 2θ at 56.536 °(110) associated. The diffraction patterns can be indexed to the hexagonal wurtzite phase, which corresponds to (marked peaks, as per JCPDS card No. 96-900-4180). The results demonstrated the increase in peak intensity with increasing ZnO content. This investigation is closely reported by [43].

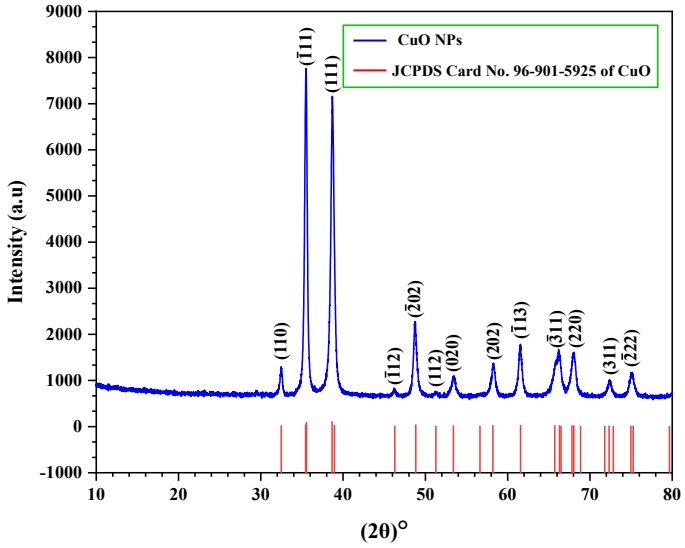

Figure 1 The plot of XRD analysis for CuO nanopowder.

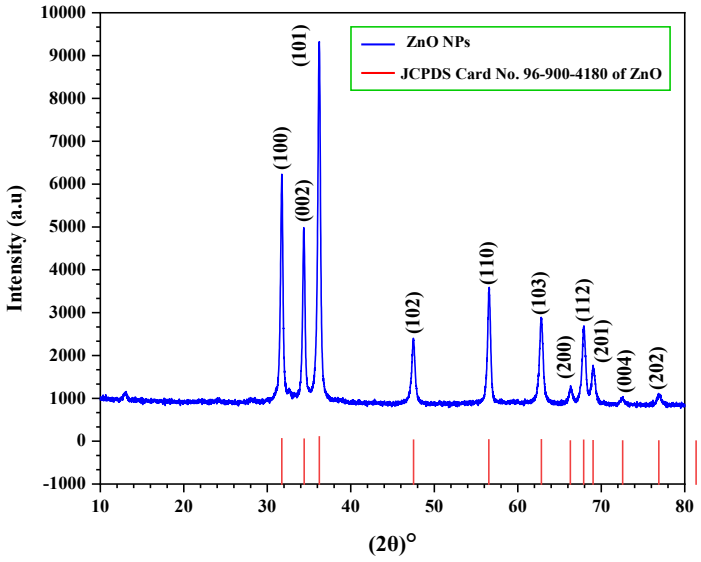

Figure 2 The plot of XRD analysis for ZnO nanopowder.

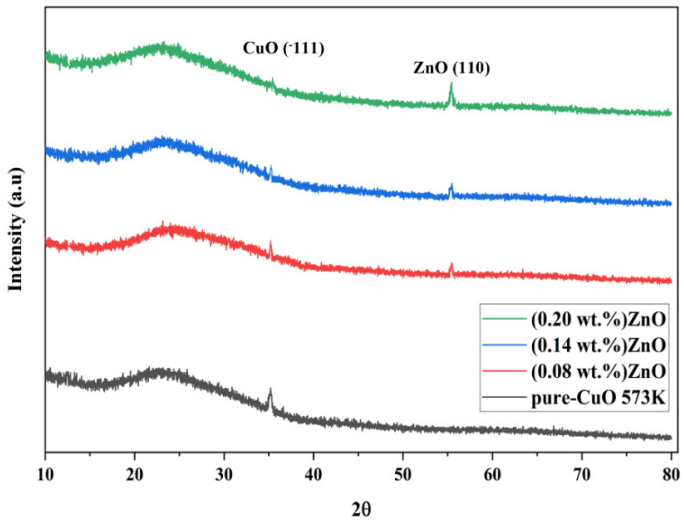

Figure 3 The plot of XRD analysis for (CuO/ZnO) thin films at 573K.

Atomic Force Microscope (AFM) measurements of (CuO/ZnO) nanocomposites

AFM pictures of 4 thin films of (CuO/ZnO) on glass substrates (6×6 μm^2) are shown in **Figure 4**. Increased ZnO nanoparticle concentration increases film crystallinity and grain size. After annealing at 573 K, the AFM image indicated a grain size increase from 75.18 to 151.81 nm as ZnO nanoparticle concentration increased from 0.08 to 0.20 wt.%. **Table 1** shows film surface roughness as root mean square (RMS) values. While annealing at 573 K, increasing ZnO nanoparticle concentration increases RMS roughness average from 12.6 to 29.7 nm and then decreases to 27.4 and 16.8 nm [37].

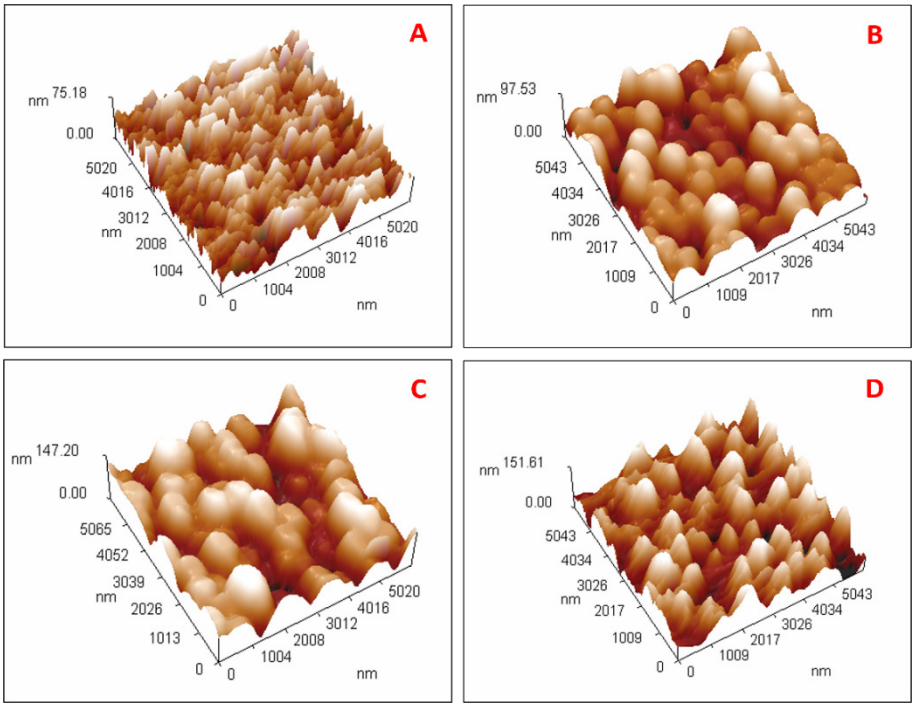

Figure 4 AFM surface morphology of (CuO/ZnO) NCs: (A) Pure CuO annealing 573 K, (B) 0.8 wt.% ZnO NPs, (C) 0.14 wt.% ZnO NPs, and (D) 0.20 wt.% ZnO NPs.

Table 1 Morphological characteristics of 573 K-annealed (CuO/ZnO) thin films.

ZnO-doped CuO Con. of wt.%	Root mean square S_q (nm)	Roughness average Sa (nm)	Ten-point heigh S_z (nm)	Average diameter (nm)
Pure (CuO)	15.9	12.6	75.18	219.4
0.08 wt.% ZnO	20.8	16.8	97.53	644.3
0.14 wt.% ZnO	32.2	27.4	147.20	688.3
0.20 wt.% ZnO	35.7	29.7	151.81	362.1

Scanning Electron Microscope (FESEM)

Measurements of (CuO/ZnO) Nanocomposites Scanning electron microscopy is a convenient technique widely used to obtain the surface morphological information of thin films. Surface morphology of (CuO/ZnO) thin films was observed using FESEM under 500 nm. Field Emission FESEMs use a high-energy electron beam to scan a sample to create pictures. Signals from electron-atom interactions disclose sample features like electrical conductivity, surface topography, and chemical composition. Thus, Scanning Electron Microscopy examined ZnO nanoparticle surface shape and size. The SEM picture revealed the presence of both individual ZnO nanoparticles and a significant quantity of aggregates [44]. **Figure 5** shows nanoparticles in thin films under study. At lower chemical concentrations, nanoparticles aggregate, explaining these observations. CuO nanoparticles can promote the formation of a network when there is a greater interaction with ZnO nanoparticles. Initially, the size of the nanoparticles increases from 219.4 to 688.3 nm for pure CuO to 0.14 wt% ZnO and decreases to 362.1 nm for 0.20 wt% ZnO The arrangement of particles indicates the presence of co-granular structures [45,46].

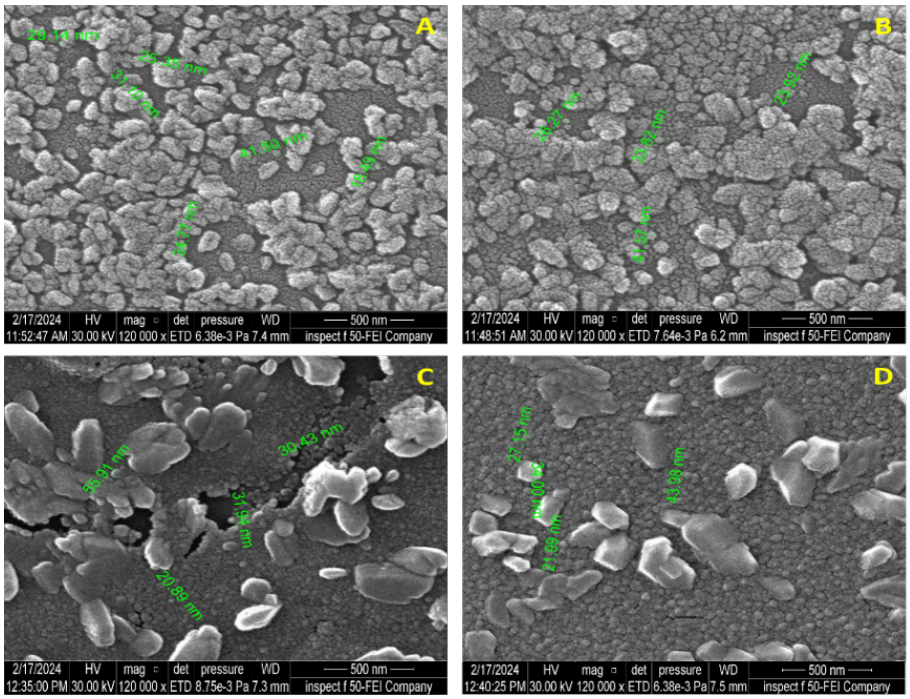

Figure 5 FESEM images of (CuO/ZnO) NCs: (A) Pure, (B) 0.08 wt.% ZnO, (C) 0.14 wt.% ZnO and (D) 0.20 wt.% ZnO for annealing 573 K.

Optical characteristics of (CuO/ZnO) nano composites

UV-Vis spectroscopy is a significant non-destructive technique used to determine the energy gap of semiconducting nanomaterials. The energy band gap of nanomaterials is altered by the introduction of dopants, which induce crystal imperfections. **Figure 4** displays the UV-visible spectra of the produced CuO and ZnO nanomaterial. The absorbance of all the samples was measured throughout the wavelength range of 320 - 720 nm. The absorbance of nanomaterial is influenced by various parameters, including impurity centers, particle size, oxygen vacancies, micro-strain, dislocation density, and film thickness [47]. CuO/ZnO absorption with variable concentration (ZnO) and wavelength range at normal temperature. (CuO/ZnO) optical absorption varies with wavelength, as shown in **Figure 6**. These statistics imply that all films have higher UV absorption spectra. The nan composites exhibit a noticeable lack of absorbance in the visible spectrum. To provide further elucidation, we can approach this matter from the following perspective: Photons of high frequencies do not undergo interactions with atoms, resulting in their transmission rather than obstruction. Photons are absorbed by substances around the fundamental absorption edge as light wavelength decreases. Increasing ZnO weight percentages boosts absorption. This happens because unbound electrons absorb light. These results match those of other researcher [48].

Figure 7 displays the wavelength-dependent transmittance (T) of (CuO/ZnO) thin films. The optical transmittance spectra of thin films with different ZnO nanoparticle concentrations were examined. The wavelength-transmittance relationship is obvious since ZnO nano-doping concentration impacts transmittance. Specifically, when the wavelength increases, the transmittance also increases, while the transmittance decreases with an increase in the concentration of ZnO nano-doping [49]. The results presented here align with the findings of other researcher [50]. A reduction in transmission resulted from the formation of oxygen vacancies and scattering at the grain boundaries. Nevertheless, the films' absorbance might fluctuate due to factors such as particle size, oxygen deprivation, and flaws in grain structures, which are influenced by the doping components [43].

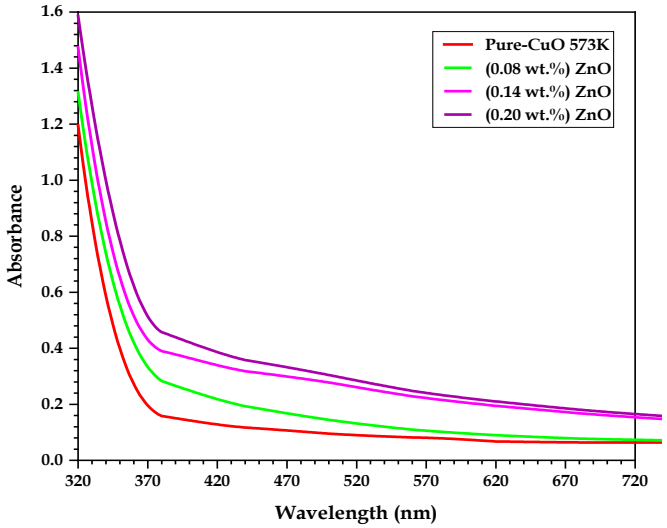

Figure 6 The absorbance spectra as a function of wavelength of (CuO/ZnO) thin films.

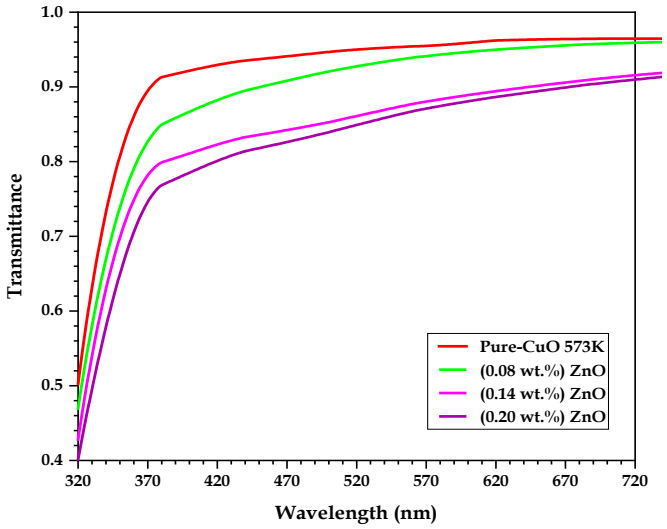

Figure 7 Transmittance spectra as a function of the wavelength of (CuO/ZnO) thin films.

Figure 8 shows the wavelength-absorption coefficient connection for CuO/ZnO thin films. Lower energy and minimal absorption coefficient are seen at longer wavelengths. The photon's insufficient energy prevents electrons from moving from the valence band to the conduction band in non-semiconductor materials [51]. At high energies, absorption is highly efficient, indicating a significant likelihood of electron transitions. Therefore, the incident photon possesses enough energy to compel the movement of a single electron from the valence band to the conduction band. The observed photon's energy exceeded the permissible energy gap [52]. Direct electron transitions occur. At high energies ($\alpha > 10^4$) cm^{-1}, the coefficient of absorption is smaller, showing constant energy and momentum for electrons and photons during the transition. Absorption coefficient values ($\alpha < 10^4$) cm^{-1} are expected at low energies, causing indirect electron transitions. The phonon helps preserve electrical momentum [53]. One of the outcomes is that the absorption coefficient of the thin film (CuO/ZnO) is larger than 10^4 cm^{-1}. This demonstrates that electron exchanges occur in a straightforward manner. This outcome is comparable to the findings of the other researcher [49].

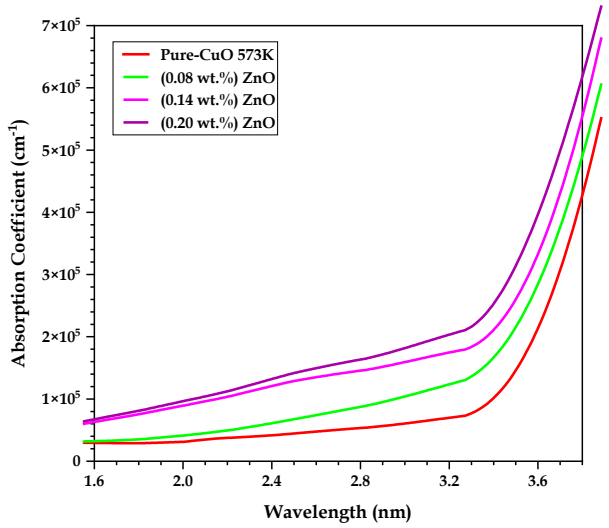

Figure 8 The absorption coefficient spectra as a function of wavelength of (CuO/ZnO) thin films.

Calculate glass samples' optical band gap using this Eq. (8) [54], where B represents a constant, while hυ represents the energy of the incident photon. The optical transitions (n = 2, 1/2, 3, and 1/3) can be classified as either indirect allowed, direct allowed, prohibited indirect, or forbidden direct transitions [55]. The absorption edge $(\alpha h\nu)^2$ for the (CuO/ZnO) material is depicted in **Figure 9**. It illustrates the relationship between the amount of photon energy and the position on the upper half of the curve where the $(\alpha h\nu)^2 = 0$ value is obtained, moving towards the x-axis. The energy gap of pure CuO and ZnO-doped CuO with thicknesses of 50 nm and ratios of 0.08, 0.14, and 0.20 wt.% is shown. As the ZnO ratio grows, the energy gap decreases. The band gap values for the generated nanofilm reduced from 3.608 to 3.504 eV for allowed direct transitions and from 3.408 to 3.161 eV for authorized indirect transitions. The optical energy gap decreases after annealing due to the introduction of additional energy levels within the forbidden gap and near the conduction band as presented in **Figure 10**. This decrease is attributed to the heat, which reduces the energy needed for direct electronic transitions and facilitates the movement of electrons from the valence to the conduction band, as shown in **Figure 11**. These results demonstrate a strong concurrence with the discoveries of researcher [56] as shown in **Table 2.**

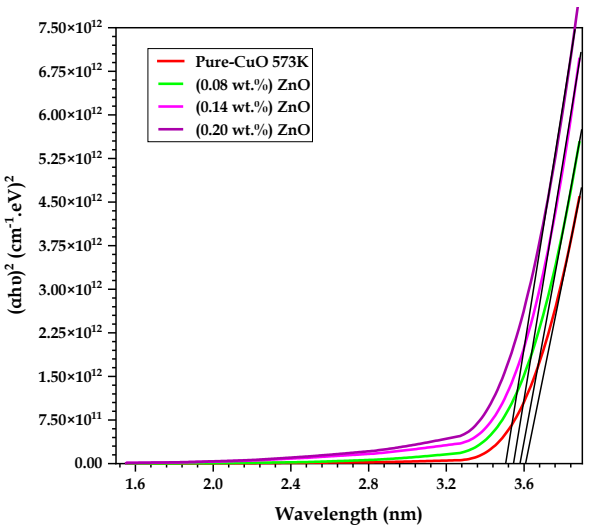

Figure 9 A plot of $(\alpha h\upsilon)^2$ verses photon energy (hυ) of (CuO/ZnO) thin films at different ZnO-doping ratios.

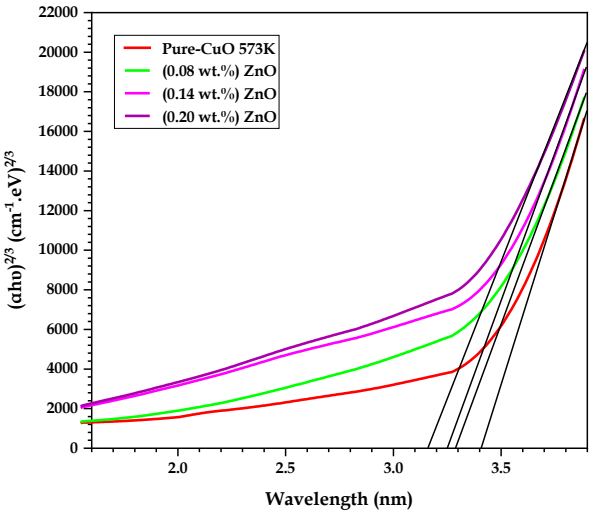

Figure 10 A plot of $(\alpha h\upsilon)^{2/3}$ verses photon energy ($h\upsilon$) of (CuO/ZnO) thin films at different ZnO-doping ratios.

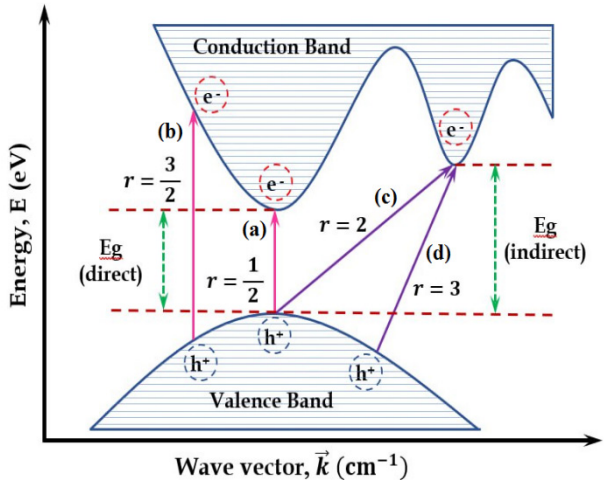

Figure 11 The types of transition (a) allowed direct, (b) forbidden direct, (c) allowed indirect and (d) forbidden indirect [57].

Table 2 Energy gap values for permitted and disallowed direct transitions in (CuO/ZnO) thin films.

ZnO-doped CuO (wt.%)	E_g(eV)	
	Allowed	Forbidden
0	3.608	3.408
0.08	3.578	3.288
0.14	3.544	3.249
0.20	3.504	3.161

Eq. (9) is used to determine the refractive index (n) of CuO and CuO/ZnO nanofilms. The investigation and analysis of the variation of the refractive index with wavelength were conducted for pure and ZnO-doped CuO nanofilms with varied doping ratios of ZnO. The films were made at RT. The results are presented in **Figure 12**.

The data indicates that the refractive index of ZnO nanofilms, both pure and doped with CuO, rises as the thickness and doping of ZnO increase. The behavior can be explained by the rise in absorbance or

absorption coefficient. Higher levels of doping lead to an elevation in the refractive index. Put simply, when light from an incoming source interacts with a material containing a large number of particles, the refractive index of the films is elevated. This aligns with the conclusions drawn by the researchers [58].

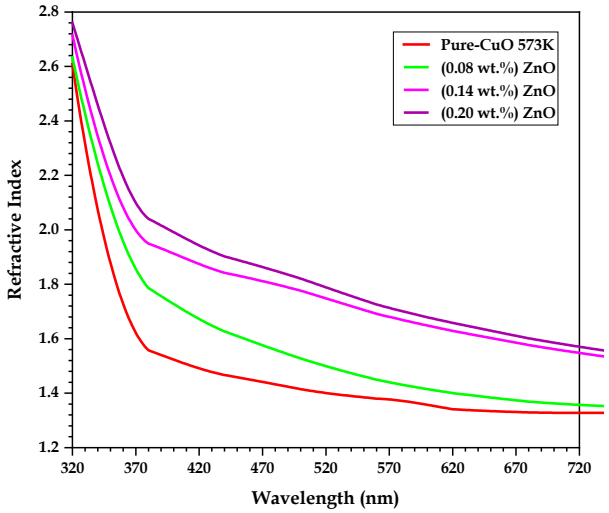

Figure 12 The refractive index spectra as a function of wavelength of (CuO/ZnO) thin films.

Figure 13 displays the relationship between optical conductivity and wavelength for thin films of (CuO/ZnO). Eq. (10) was employed to compute the optical conductivity. The figure shows that all thin film samples' optical conductivity decreases with wavelength. The wavelength of incident light determines thin film sample optical conductivity, explaining this behavior. Thin film samples absorb more light at low wavelengths, increasing optical conductivity. This boosts charge transfers excitations.

The optical conductivity spectra showed that the materials transmit visible and near-infrared light. Thin film optical conductivity increases with ZnO nanoparticle concentrations. This behavior is caused by localized energy levels in the energy gap. The density of these localized levels in the band structure increases with ZnO nanoparticle concentration. This raises the absorbance coefficient and optical conductivity of (CuO/ZnO) thin films. They match the researcher's findings [59,60].

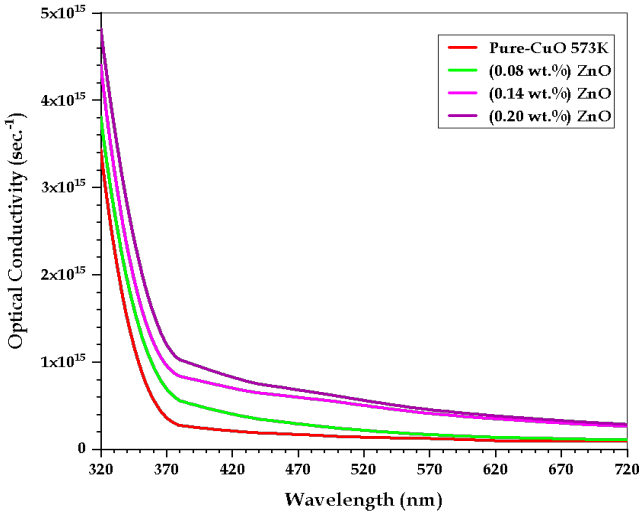

Figure 13 The optical conductivity spectra as a function of wavelength of (CuO/ZnO) thin films.

Application of (CuO/ZnO) thin films as gas sensors

A stainless-steel cylindrical examination chamber with a 20 cm diameter and 10 cm height makes up the gas sensor system. The compartment is emptied by a rotary pump. The device has a verified gas inlet and an air admittance valve for ambient air after evacuation. The chamber base has a multi-pin feed-through for thermocouples, sensor electrodes, and heater connections. A GEMO DT109 PID temperature controlled sensor temperature. A hot plate heater was controlled by a type K thermocouple inside the chamber. A laptop computer tracks the sensor's resistance changes during gas exposure. Vector 70 C is a PC-interfaced digital multimeter that measures resistance. Gas is fed through a tube above the sensor in the test chamber to ensure exact sensitivity and evaluate sensor resistance changes after exposure to air and NO_2. With a needle valve and flow meters, circulation is achieved. **Figure 14** shows the gas sensor system.

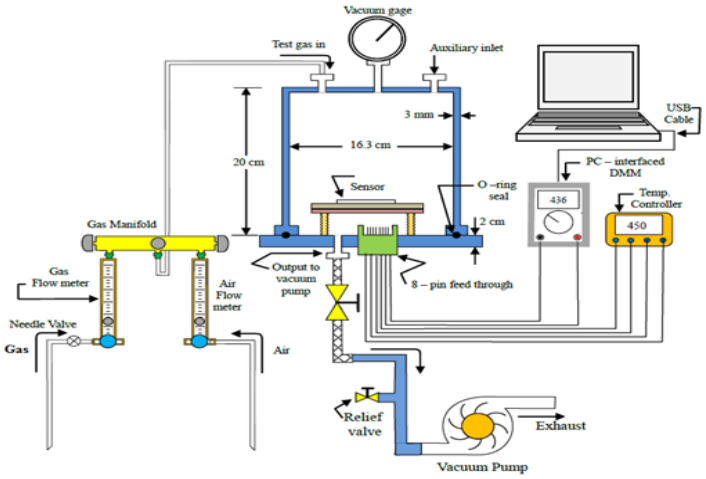

Figure 14 Gas sensing apparatus schematic diagram.

Figures 15 - 17 shows electrical resistance when needle valves open or close gas vapor time at RT, 100 and 200 °C. Continuous 500 ppm NO_2 gas injection into the testing chamber. This is done with ambient air at each sample's operating temperature. Over time, the resistance is evaluated and stabilized before gas flow begins. Gas is cut off when resistance spikes to a constant. The electrical resistance reset. Gas molecules interact with the detecting film's surface atoms to determine the sensor's gas detection ability. All samples' electrical resistance was measured by the computer. Computerized measurements were taken. A multimeter, specifically the Vector 70C model, is linked to an interface. The CuO/ZnO, nanofilms sensor, was fabricated and evaluated at different operating temperatures [61].

The data presented in **Figures 15 - 17** of the nanofilm sensors demonstrate p-type semiconducting behavior, as seen by the negative connection between electrical resistance and time. As an illustration, the electrical resistance exhibited a decrease upon activation of an oxidizing gas, such as NO_2. Furthermore, the resistance had a negative correlation with time during the gas activation. The value consistently and progressively rose and thereafter fully returned to its original state following the presence of NO_2. The gas supply was cut off due to NO_2, a chemical oxidant. P-type semiconductor nanofilm sensors can accept electrons from the valence band when NO_2 is present. This increases charge carrier concentration, particularly holes. Thus, electrical conductivity increases, and resistance decreases. NO_2 adsorption onto p-type semiconductors at 0.08, 0.14, and 0.20 wt.% improves nanofilm sensor performance. NO_2, a chemical oxidant, changes sensor properties. Thus, NO_2 gas lowers the electrical resistance of all nanofilm-based sensor samples. A reducing gas like NH_3 reverses the electrical resistance change in NO_2 exposed to an oxidizing gas. Oxygen ions on the nanofilm sensor surface produced NO_2- once NO_2

molecules were introduced. This occurred with nanofilm sensors of Pure, 0.08, 0.14, and 0.20 wt.% weight. They are associated with surface grain interfaces. A sealed gas vapor increases electrical resistance. Once NO_2 is removed, resistance returns to R air. This happens because NO_2- reacts with oxygen ions absorbed at grain boundaries. This process decreases hole density and electrical conductivity, increasing electrical resistance. Another study found a similar phenomenon [62].

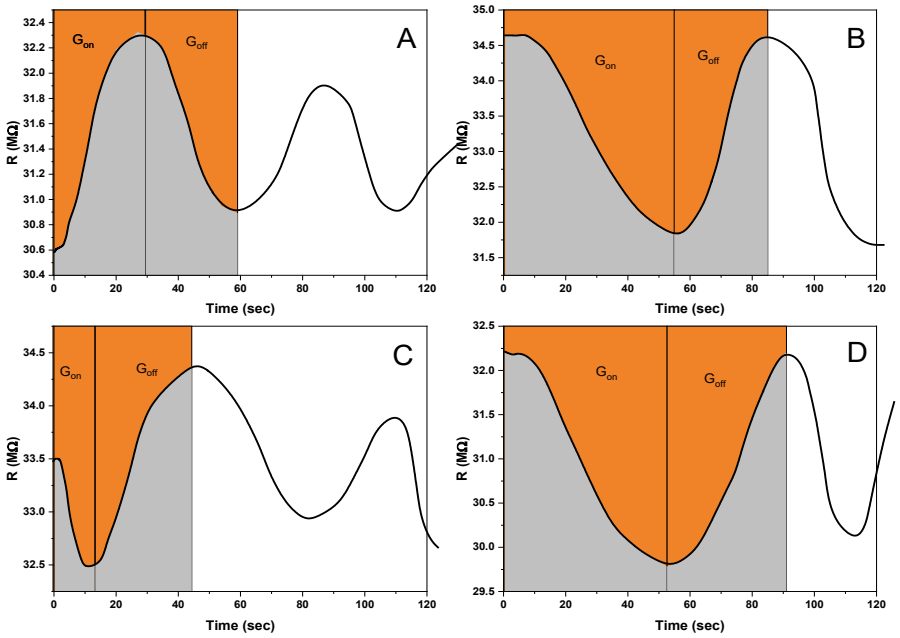

Figure 15 Plot of relationship between resistance with time of: (A) Pure (CuO), (B) 0.08 wt.%, (C) 0.14 wt.%, and (D) 0.20 wt.% ZnO thin film sensors exposed to NO_2 gas at RT.

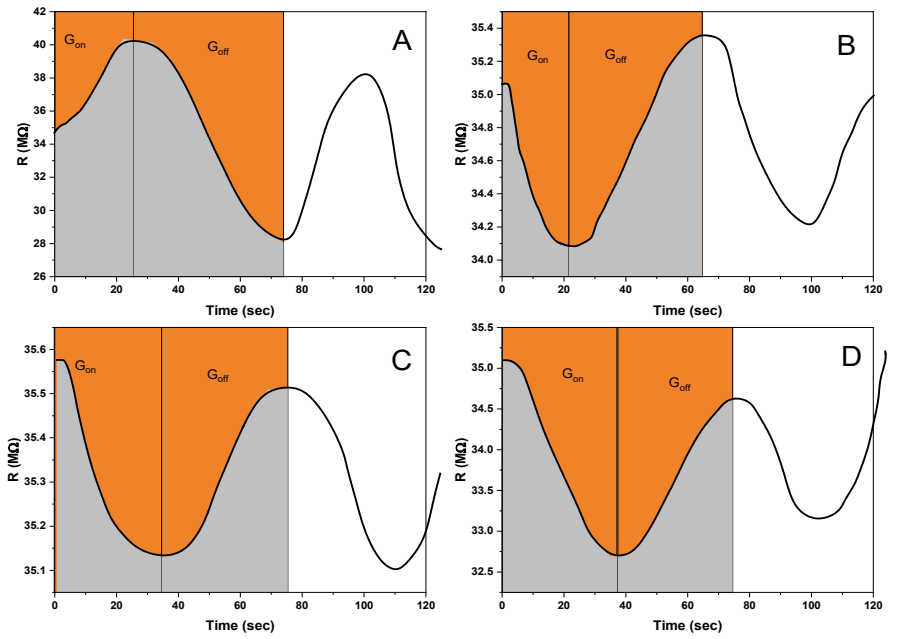

Figure 16 Plot of relationship between resistance with time of: (A) Pure (CuO), (B) 0.08 wt.%, (C) 0.14 wt.%, and (D) 0.20 wt.% ZnO thin film sensors exposed to NO_2 gas at 100 °C.

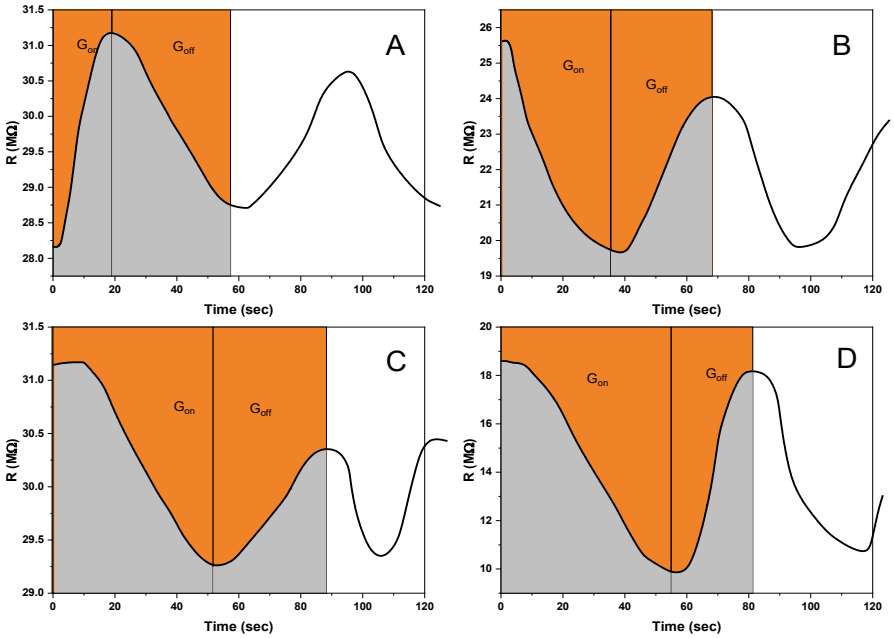

Figure 17 Plot of relationship between resistance with time of: (A) Pure (CuO), (B) 0.08 wt.%, (C) 0.14 wt.%, and (D) 0.20 wt.% ZnO thin film sensors exposed to NO_2 gas at 200 °C.

Figure 18 shows that the 0.20 wt.% maximal sensitivity to NO_2 at 100 was 47.06 %, with a reaction time of 36.00 s and a recovery time of 19.8 s. Sample sensitivity (0.20 wt.%) decreases with temperature. This shows that the gas sensor interacts with NO_2 gas via physical adsorption and polarity without activation energy. Prior research supports this action [63]. However, the Pure, 0.08 and 0.14 wt.% samples' sensitivity correlated positively with temperature within a certain range. Thus, the gas sensor needs energy to interact with NO_2 gas and has increased sensitivity.

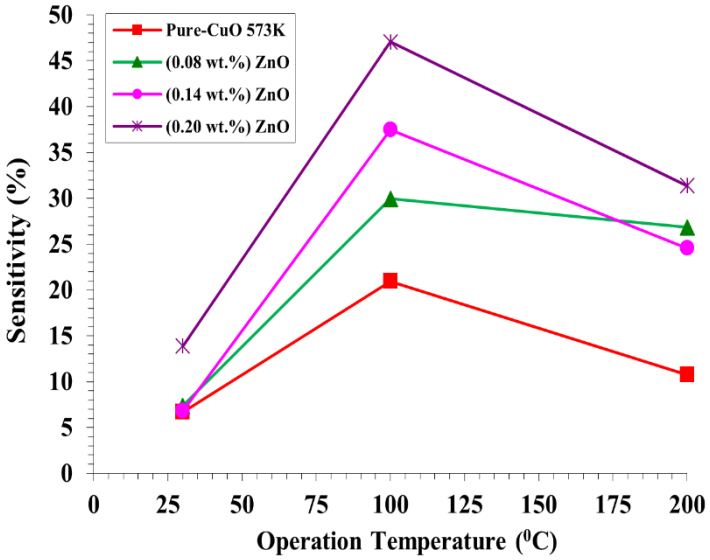

Figure 18 The sensitivity of (CuO/ZnO) nan composites at 500 ppm for NO_2 gas sensors is plotted against operation temperature.

Variable concentrations have variable reaction and recovery durations due to operation temperatures. Response time is the time it takes the sample to react to the gas, whereas prompt recovery is the time it takes the sample to return to its original state, as shown in **Figure 14** [39]; see **Table 3**.

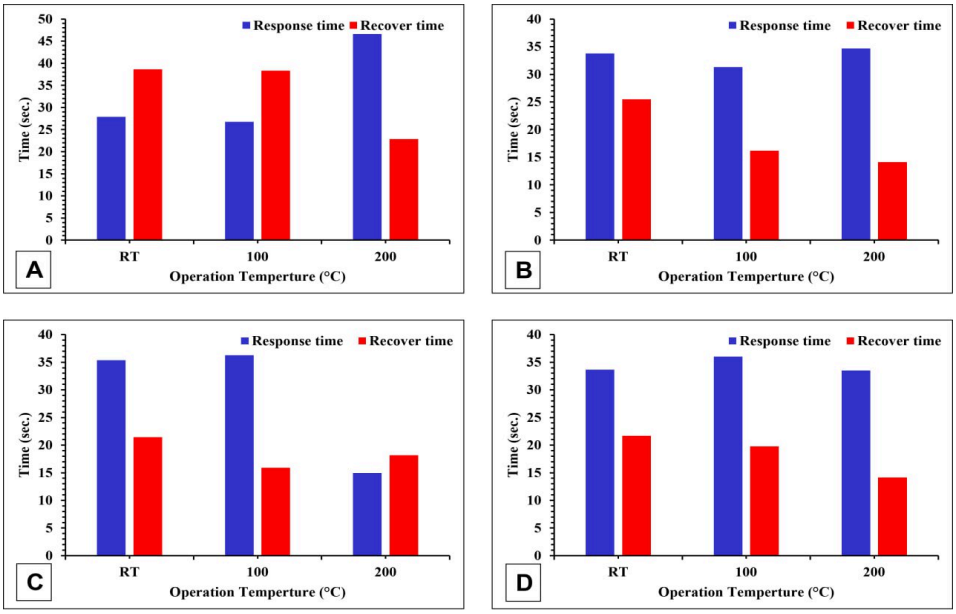

Figure 19 Response and recovery time plotted with operation temperature for (CuO/ZnO) nanocomposites: (A) Pure, (B) 0.08 wt.%, (C) 0.14 wt.%, and (D) 0.20 wt.% at 500 ppm concentration for NO_2 gas sensor.

Table 3 The gas sensor properties of (CuO/ZnO) thin films at 573 K indicate the presence of NO_2 gas.

Con. of ZnO doping in CuO (wt.%)	Operation Temp. (°C)	Sensitivity (%)	Response time (s)	Recovery time (s)
Pure	RT	6.70	27.90	38.61
	100	20.94	26.73	38.34
	200	10.77	46.62	22.86
0.08	RT	7.36	33.75	25.47
	100	29.95	31.32	16.20
	200	26.81	34.65	14.13
0.14	RT	6.81	35.37	21.42
	100	37.47	36.27	15.93
	200	24.55	14.94	18.18
0.20	RT	13.87	33.66	21.69
	100	47.06	36.00	19.80
	200	31.37	33.48	14.13

The practical results of the proposed research were compared with previous works as presented in **Table 4** in order to show the most important results and improvements obtained during the research, which show the most important strengths compared to previous works.

Table 4 The comparison of the proposed work with previous works.

Nanocomposites of sensor	Operating Temp. (°C)	Target gas/vapor	Concentrations of No_2 gas (ppm)	Response time (s)	Recovery time (s)	Sensor sensitivity (%)	Ref.
rGO/ZnO	RT	NO_2	5 (1 - 25)	165	499	25.6	[29]
rGO/ZnO-Au	80 (60 - 90)	NO_2	100 (20 - 100)	27	86	32.55	[30]
Ni@ZnO/PANi	RT	NO_2	100	82	399	75	[31]
CuO-ZnO	200	NO_2	100	5	280	73	[32]
CuO/ZnO	100	NO_2	500	36	19.8	47.06	This work

Conclusions

This paper describes the preparation of thin films using pure CuO and ZnO-doped CuO with different contents of (0, 0.8, 0.14, and 0.20 wt.%). After deposition, the films were annealed at 573 K for 2 h. XRD analysis proved that CuO is monoclinic wurtzite-type with the presence of ZnO in the prepared films. As ZnO doping increased, crystallite size increased. Thin film AFM pictures showed a constant granular surface shape. As ZnO doping increased, the roughness average and root mean square increased. The optical characteristics of (CuO/ZnO) show that the absorbance and absorption coefficient increase with ZnO content. The transmittance and energy band gaps decreased as ZnO concentrations increased, which absorbed UV radiation. A direct energy gap (E_g) reduced from 3.608 to 3.504 eV when ZnO doping increased in the optical test of pure and Cu-doped ZnO thin films. The negative correlation between electrical resistance and time indicates p-type semiconducting nanofilm sensors. When exposed to NO_2 gas, nanofilm sensor samples have lower electrical resistance. Gas sensors with a thin CuO/ZnO layer performed better at 100 °C. Gas detection sensitivity was 47.06 % in the study. NO_2 gas raised operating temperature. Followed by faster response and recovery.

Acknowledgements

The authors would like to produce appreciate and thanks to the anonymous reviewers and editor(s) of the journal. In addition, the authors thanks Babylon University, Iraq, for their support.

References

[1] MH Meteab, A Hashim and BH Rabee. Synthesis and structural properties of (PS-PC/Co_2O_3-SiC) nanocomposites for antibacterial applications, nanosistemi, nanomater. *Nanosistemi Nanomateriali Nanotehnologii* 2023; **21**, 451-460.

[2] MG Lines. Nanomaterials for practical functional uses. *Journal of Alloys and Compunds* 2008; **449(1-2)**, 242-245.

[3] A Fadaka, O Aluko, S Awawu and K Theledi. Green synthesis of gold nanoparticles using pimenta dioica leaves aqueous extract and their application as photocatalyst, antioxidant, and antibacterial agents. *Journal of Multidisciplinary Applied Natural Science* 2021; **1(2)**, 78-88.

[4] LA Kolahalam, IVK Viswanath, BS Diwakar, B Govindh, V Reddy and YKN Murthy. Review on nanomaterials: Synthesis and applications. *Materials Today: Proceedings* 2019; **18**, 2182-2190.

[5] HS Nalwa. *Handbook of nanostructured materials and nanotechnology*. Academic Press, Cambridge, 1999.

[6] S Logothetidis. *Nanostructured materials and their applications.* Springer Berlin, Heidelberg, Germany, 2012.

[7] E Omanović-Mikličanin, A Badnjević, A

Kazlagić and M Hajlovac. Nanocomposites: A brief review. *Health and Technology* 2020; **10**, 51-59.

[8] V Khoramshahi, M Azarang, M Nouri, A Shirmardi and R Yousefi. Metal oxide/g-C_3N_4 nanocomposites chemiresistive gas sensors: A review on enhanced performance. *Talanta Open* 2024; **9**, 100290.

[9] KMMA El-Nour, A Eftaiha, A Al-Warthan and RAA Ammar. Synthesis and applications of silver nanoparticles. *Arabian Journal of Chemistry* 2010; **3(3)**, 135-140.

[10] NA Ibrahim. *Nanomaterials for antibacterial textiles*. *In*: M Rai and K Kon (Eds.). Nanotechnology in diagnosis, treatment and prophylaxis of infectious diseases. Academic Press, Cambridge, 2015, p. 191-216.

[11] Z Yang, H Peng, W Wang and T Liu. Crystallization behavior of poly(ε-caprolactone)/layered double hydroxide nanocomposites. *Journal of Applied Polymer Science* 2010; **116(5)**, 2658-2667.

[12] MH Abbas, H Ibrahim, A Hashim and A Hadi. Fabrication and tailoring structural, optical, and dielectric properties of PS/$CoFe_2O_4$ nanocomposites films for nanoelectronics and optics applications. *Transactions on Electrical and Electronic Materials* 2024; **25**, 449-457.

[13] S Murthy, P Effiong and CC Fei. *Metal oxide nanoparticles in biomedical applications*. *In*: Y Al-Douri (Ed.). Metal oxide powder technologies: Fundamentals, processing methods and applications. Elsevier, Amsterdam, The Netherlands, 2020, p. 233-251.

[14] GA Kontos, AL Soulintzis, PK Karahaliou, GC Psarras, SN Georga, CA Krontiras and MN Pisanias. Electrical relaxation dynamics in TiO_2 - polymer matrix composites. *Express Polymer Letters* 2007; **1(12)**, 781-789.

[15] S Laurent, S Boutry and RN Muller. *Metal oxide particles and their prospects for applications. In*: M Mahmoudi and S Laurent (Eds.). Iron oxide nanoparticles for biomedical applications: Synthesis, functionalization and application. Elsevier, Amsterdam, The Netherlands, 2018, p. 3-42.

[16] J Lillo-Ramiro, JM Guerrero-Villalba, MDL Mota-González, FS Aguirre-Tostado, G Gutiérrez-Heredia, I Mejía-Silvan and A Carrillo-Castillo. Optical and microstructural characteristics of CuO thin films by sol gel process and introducing in non-enzymatic glucose biosensor applications. *Optik* 2021; **229**, 166238.

[17] R Nayak, FA Ali, DK Mishra, D Ray, VK Aswal, SK Sahoo and B Nanda. Fabrication of CuO nanoparticle: An efficient catalyst utilized for sensing and degradation of phenol. *Journal of Materilals Research and Technology* 2020; **9(5)**, 11045-11059.

[18] ME Grigore, ER Biscu, AM Holban, MC Gestal and AM Grumezescu. Methods of synthesis, properties and biomedical applications of CuO nanoparticles. *Pharmaceuticals* 2016; **9(4)**, 75.

[19] C Wang, XQ Fu, XY Xue, YG Wang and TH Wang. Surface accumulation conduction controlled sensing characteristic of p-type CuO nanorods induced by oxygen adsorption. *Nanotechnology* 2007; **18(14)**, 145506.

[20] N Mukherjee, B Show, SK Maji, U Madhu, SK Bhar, BC Mitra, GG Khan and A Mondal. CuO nano-whiskers: Electrodeposition, Raman analysis, photoluminescence study and photocatalytic activity. *Materilats Letters* 2011; **65(21-22)**, 3248-3250.

[21] N Mukherjee, A Mondal and U Madhu. Chemical bath deposition of thin films of CuO nanorods and their characterisation. *International Journal of Nanomanufacturing* 2010; **5(1-2)**, 16-24.

[22] SK Maji, N Mukherjee, A Mondal, B Adhikary and B Karmakar. Chemical synthesis of mesoporous CuO from a single precursor: Structural, optical and electrical properties. *Journal of Solid State Chemistry* 2010; **183(8)**, 1900-1904.

[23] J Morales, L Sánchez, F Martín, JR Ramos-Barrado and M Sánchez. Use of low-temperature nanostructured CuO thin films deposited by spray-pyrolysis in lithium cells. *Thin Solid Films* 2005; **474(1-2)**, 133-140.

[24] T Itoh and K Maki. Growth process of CuO(111) and Cu_2O(001) thin films on MgO(001) substrate under metal-mode condition by reactive dc-magnetron sputtering. *Vacuum* 2007; **81(9)**,

1068-1076.

[25] IY Erdoğan and Ö Güllü. Optical and structural properties of CuO nanofilm: Its diode application. *Journal of Alloys and Compounds* 2010; **492(1-2)**, 378-383.

[26] A Moezzi, AM McDonagh and MB Cortie. Zinc oxide particles: Synthesis, properties and applications. *Chemical Engineering Journal* 2012; **185-186**, 1-22.

[27] R Chen, Z Li and W Gao. Effect of substrate on the morphology, crystal structure and property of ZnO thin films. *Asia-Pacific Journal of Chemical Engineering* 2007; **2(5)**, 388-393.

[28] HS Suhail and AR Abdulridha. Synthesis, optical and AC electrical characteristics of nanocomposites (Bi_2O_3/ZnO) films prepared by thermal evaporation technique. *Digest Journal of Nanomaterials and Biostructures* 2023; **18(2)**, 437-450.

[29] S Liu, B Yu, H Zhang, T Fei and T Zhang. Enhancing NO_2 gas sensing performances at room temperature based on reduced graphene oxide-ZnO nanoparticles hybrids. *Sensors and Actuators B: Chemical* 2014; **202**, 272-278.

[30] TT Tung, NV Chien, NV Duy, NV Hieu, MJ Nine, CJ Coghlan, DNH Tran and D Losic. Magnetic iron oxide nanoparticles decorated graphene for chemoresistive gas sensing: The particle size effects. *Journal of Colloid and Interface Science* 2019; **539**, 315-325.

[31] SM Mali, SS Narwade, YH Navale, SB Tayade, RV Digraskar, VB Patil, AS Kumbhar and BR Sathe. Heterostructural CuO-ZnO Nanocomposites: A highly selective chemical and electrochemical NO_2 sensor. *ACS Omega* 2019; **4(23)**, 20129-20141.

[32] S Jain, N Karmakar, A Shah and NG Shimpi. Development of Ni doped ZnO/polyaniline nanocomposites as high response room temperature NO_2 sensor. *Materials Science and Engineering: B* 2019; **247**, 114381.

[33] NA Hassan and IH Khudayer. Study of the structural and optical properties of CuAlxIn1-xTe2 thin film. *AIP Conference Proceedings* 2019; **2190(1)**, 20050.

[34] N Hayder, A Hashim, MA Habeeb, BH Rabee, AG Hadi and MK Mohammed. Analysis of dielectric properties of PVA/PEG/In_2O_3 nanostructures for electronics devices. *Journal of Composite and Advanced Materials* 2022; **32(5)**, 261-264.

[35] MK Mohammed, TN Khudhair, KS Sharba, A Hashim, QM Hadi and MH Meteab. Tuning the morphological and optical characteristics of SnO_2/ZrO_2 nanomaterials doped PEO for promising optoelectronics applications. *Journal of Composite and Advanced Materials* 2024; **34(4)**, 495-503.

[36] GW Luckey. Introduction to solid state physics. *Journal of the American Chemical Society* 1957; **79(12)**, 3299.

[37] L Leontie, M Caraman, M Delibaş and GI Rusu. Optical properties of bismuth trioxide thin films. *Materials Research Bulletin* 2001; **36(9)**, 1629-1637.

[38] L Zhang, Y Hashimoto, T Taishi, I Nakamura and QQ Ni. Fabrication of flower-shaped Bi_2O_3 superstructure by a facile template-free process. *Applied Surface Science* 2011; **257**, 6577-6582.

[39] WK Mahmood, TM Rashid, MI Rahmah, AM Jasim, MQ Fahem, MS Jabir, DA Abid, RA Majed, DM Awaid and HM Yosif. Empowering NO_2 detection: Synthesis of highly responsive Au/Cu-doped iron oxide nanoparticles as gas sensors through laser ablation. *Plasmonics* 2024. https://doi.org/10.1007/s11468-024-02235-2.

[40] MH Sarfi, M Ghadimi and A Babaee. H_2S gas sensor based on SnO_2 and CuO nanoparticles. *STEM Fellowship Journal* 2015; **1(2)**, 21-26.

[41] NH Harb and FAH Mutlak. Gas sensing characteristics of WO3NPs sensors fabricated by pulsed laser deposition on PS n-type. *Journal of Optics* 2022; **52**, 323-331.

[42] KH Abass and MK Mohammed. Fabrication of ZnO:Al/Si solar cell and enhancement its efficiency via AI-doping. *Nano Biomedicine and Engineering* 2019; **11(2)**, 170-177.

[43] SS Zahirullah, JJ Prince and PFH Inbaraj. Structural and optical properties of Cu-doped ZnO nanorods by silar method. *Materials Technology* 2017; **21**, 38.

[44] HK Obayes, MH Meteab and BA Al-Kareem. Modified dosimetric features of new type of lithium borate glass system: Role of magnesium

and gold Co-doping. *Transactions on Electrical and Electronic Materials* 2024; **25**, 708-721.

[45] M Yasin, M Saeed, M Muneer, M Usman, AU Haq, M Sadia and M Altaf. Development of Bi_2O_3-ZnO heterostructure for enhanced photodegradation of rhodamine B and reactive yellow dyes. *Surfaces and Interfaces* 2022; **30**, 101846.

[46] MH Naeem, SHH Al-Nesrawy and MH Al-Maamori. Influence of lead nanoparticles on structural, morphological, and mechanical characteristics of (SiR-PU/Micro-Pb) composites and radiation shielding applications. *East European Journal of Physics* 2023; **3(3)**, 539-545.

[47] RO Yathisha, YA Nayaka, P Manjunatha, HT Purushothama, MM Vinay and KV Basavarajappa. Study on the effect of Zn^{2+} doping on optical and electrical properties of CuO nanoparticles. *Physica E: Low-Dimensional Systems and Nanostructures* 2019; **108**, 257-268.

[48] R Grazziotin-Soares, MH Nekoofar, TE Davies, A Bafail, E Alhaddar, R Hübler, ALS Busato and PMH Dummer. Effect of bismuth oxide on white mineral trioxide aggregate: Chemical characterization and physical properties. *International Endodontic Joournal* 2014; **47(6)**, 520-533.

[49] MK Khalaf, BT Chiad, AF Ahmed and FAH Mutlak. Thin film technique for preparing nano-ZnO gas sensing (O_2, NO_2) using Plasma Deposition. *International Journal of Application or Innovation in Engineering & Management* 2013; **2(6)**, 178-184.

[50] W Gao and Z Li. ZnO thin films produced by magnetron sputtering. *Ceramics International* 2004; **30**, 1155-1159.

[51] Ü Özgür, YI Alivov, C Liu, A Teke, MA Reshchikov, S Doğan, V Avrutin, SJ Cho and H Morkọ. A comprehensive review of ZnO materials and devices. *Journal of Applied Physics* 2005; **98(4)**, 41301.

[52] L Cong, X Zheng, P Hu and S Dan-Feng. Bi_2O_3 vaporization in microwave-sintered ZnO varistors. *Journal of the American Ceramic Society* 2007; **90(9)**, 2791-2794.

[53] VS Kalyamwar, FC Raghuwanshi, NL Jadhao and AJ Gadewar. Zinc oxide nanostructure thick films as H_2S gas sensors at room temperature. *Journal of Sensor Technology* 2013; **3**, 31-35.

[54] GS Ahmed, TH Mahmoud, HI Mohammed and AA Hussein. Fabrication and study of ZnO thin films using thermal evaporation technique. *Egyptian Journal Chemistry* 2021; **64**, 5189-5197.

[55] I Dhahri, M Ellouze, S Labidi, QM Al-Bataineh, J Etzkorn, H Guermazi, A Telfah, CJ Tavares, R Hergenröder and T Appel. Optical and structural properties of ZnO NPs and ZnO-Bi_2O_3 nanocomposites. *Ceramics Interational* 2022; **48**, 266-277.

[56] GA Somorjai and Y Li. *Introduction to surface chemistry and catalysis*. John Wiley & Sons, New Jersey, 2010.

[57] MH Meteab, A Hashim and BH Rabee. Synthesis and tailoring the morphological, optical, electronic and photodegradation characteristics of PS-PC/MnO_2-SiC quaternary nanostructures. *Optical and Quantum Electronics* 2023; **55**, 187.

[58] M Rizwan, A Shoukat, A Ayub, B Razzaq and MB Tahir. *Types and classification of nanomaterials. In*: Nanomaterials: Synthesis, characterization, hazards and safety. Elsevier, Amsterdam, The Natherlands, 2021, p. 31-54.

[59] F Teimoori, K Khojier and NZ Dehnavi. On the dependence of H_2 gas sensitivity of ZnO thin films on film thickness. *Procedia Materials Science* 2015; **11**, 474-479.

[60] TT Liu, MH Wang and HP Zhang. Synthesis and characterization of ZnO/Bi_2O_3 core/shell nanoparticles by the sol-gel method. *Journal of Electronic Materials* 2016; **45**, 4412-4417.

[61] RA Abdul-Nabi and E Al-Bermany. Performers of Si_3N_4 concentrations on morphology and electrical behavior for new quinary fabrication PEO-CMC-PANI/GO@Si_3N_4 nanocomposites for electronic devise and gas sensor application. *Silicon* 2024; **16**, 5583-5601.

[62] WK Mahmood and AN Naje. Fabrication of room temperature NO_2 gas sensor based on silver nanoparticles-decorated carbon nanotubes. *Journal of Nano-Electronic Physics* 2018; **10(5)**, 5020.

[63] HS Suhail and AR Abdulridha. Investigation of

the morphological, optical, and D.C electrical characteristics of synthesized (Bi_2O_3/ZnO) nanocomposites, as well as their potential use in hydrogen sulfide gas sensor. *Transactions on Electrical and Electronic Materials* 2023; **24**, 205-216.